

TFNet: Exploiting Temporal Cues for Fast and Accurate LiDAR Semantic Segmentation

Rong Li¹, Shijie Li^{2*}, Xieyuanli Chen², Teli Ma¹, Hao Wang³, Juergen Gall^{2,4} and Junwei Liang^{1,5*}

Abstract—LiDAR semantic segmentation plays a crucial role in enabling autonomous driving and robots to understand their surroundings accurately and robustly. There are different types of methods, such as point-based, range-image-based, polar-based, and hybrid methods. Among these, range-image-based methods are widely used due to their efficiency. However, they face a significant challenge known as the “many-to-one” problem caused by the range image’s limited horizontal and vertical angular resolution. As a result, around 20% of the 3D points can be occluded. In this paper, we present TFNet, a range-image-based LiDAR semantic segmentation method that utilizes temporal information to address this issue. Specifically, we incorporate a temporal fusion layer to extract useful information from previous scans and integrate it with the current scan. We then design a max-voting-based post-processing technique to correct false predictions, particularly those caused by the “many-to-one” issue. We evaluated the approach on two benchmarks and demonstrate that the post-processing technique is generic and can be applied to various networks. We will release our code and models.

I. INTRODUCTION

LiDAR (light detection and ranging) semantic segmentation enables a precise and fine-grained understanding of the environment for robotics and autonomous driving applications [1], [2], [3]. There are four categories of methods: point-based [4], [5], [6], [7], [8], [9], [10], range-image-based [11], [12], [13], [14], [15], [16], polar-based [17] and hybrid methods [18], [19]. Among them, the range-image-based methods are orders of magnitude more efficient than the other methods [20], [21]. Additionally, this approach enables the direct use of well-optimized Convolutional Neural Network (CNN) models. As a result, it offers a superior trade-off between speed and accuracy, making it especially suited for LiDAR semantic segmentation.

However, the range view representation suffers from a boundary-blurring effect [15], [12]. This problem exists mainly because of the limited horizontal and vertical angular resolution: more than one point will be projected to the same range image pixel when these points share the same vertical and horizontal angle. This is also referred to as the “many-to-one” problem [12]. Considering that the projection

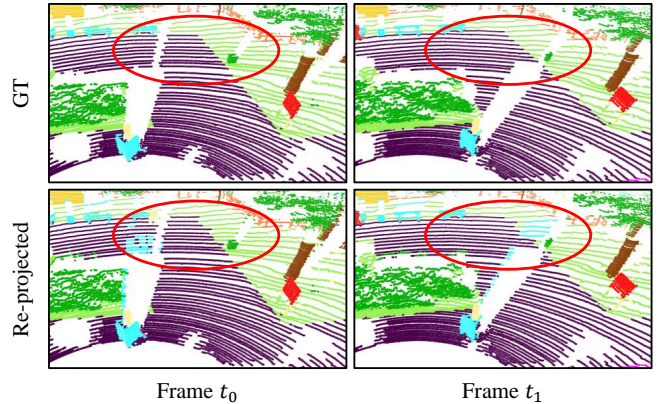


Fig. 1: Range-image-based methods suffer from the “many-to-one” problem where multiple 3D points with the same angle are mapped to a single range pixel. This can cause distant points to receive erroneous predictions (marked by the red circles) from nearby points when the range image is re-projected to 3D. Moreover, the occluded points in t_0 are visible in t_1 , which can help correct the predictions.

computes distant points first and near points later [15], the distant points will be occluded by the near points. Hence, during the re-projection of the range image into three-dimensional coordinates, a necessary procedure for range-image-based approaches, distant points will be assigned the same predicted label as the overlapping closer points. As shown in Fig. 1, this introduces errors for the distant points. In fact, we measure the impact of this phenomenon on SemanticKITTI [1], [22]. If the range image has a size of $(H, W) = (64, 2048)$, over 20% of the 3D points are occluded in the range image, i.e., more than one point is projected to the same pixel. As shown in Tab. III, this results in a substantial degradation of the accuracy if it is not addressed by an additional post-processing step. Therefore, various post-processing approaches like k-NN [15], CRF [16] or NLA [12] have been proposed. For instance, NLA [12] assigns the prediction of the nearest point to the occluded points.

In this work, we propose to incorporate temporal information to address the “many-to-one” challenge for LiDAR semantic segmentation. This is inspired by human visual perception, where temporal information is crucial for understanding object motion and identifying occlusions. This is also observed in LiDAR semantic segmentation, where heavily occluded points can be captured from adjacent range image scans, as shown in Fig. 1. Based on this intuition, we

¹Rong Li, Teli Ma and Junwei Liang are with the Hong Kong University of Science and Technology (Guangzhou), China. Email: rongli, junweiliang@hkust-gz.edu.cn

²Shijie Li, Xieyuanli Chen and Juergen Gall are with the University of Bonn, Germany. Email: lsj@uni-bonn.de

³Hao Wang is with the Alibaba Cloud Intelligence Group, China

⁴Juergen Gall is also affiliated with the Lamarr Institute for Machine Learning and Artificial Intelligence, Germany

⁵Junwei Liang is also affiliated with the Hong Kong University of Science and Technology, China

*Corresponding authors: Junwei Liang, Shijie Li

exploit the temporal relations of features in the range map via cross-attention [23], [24], [25]. As for the inference stage, we propose a max-voting-based post-processing scheme that effectively reuses the predictions of past frames. To this end, we transform the previous scans with predicted semantic class labels into the current ego car coordinate frame and then obtain the final segmentation by aggregating the predictions within the same voxel by max-voting. In summary, we make the following three contributions:

- We propose TFNet, a range-based LiDAR semantic segmentation method. It utilizes a temporary cross-attention layer, which extracts informative features from previous LiDAR scans and combines them with current range features, to compensate for occluded objects.
- We design a temporal-based post-processing method to solve the “many-to-one” mapping issue in range images. Compared with previous post-processing steps, our method achieves better performance, which is verified for various networks.
- We evaluate the proposed method on two public benchmarks, namely SemanticKITTI [1] and SemanticPOSS [26], where our method achieves a good trade-off between accuracy and inference time.

II. RELATED WORK

LiDAR semantic segmentation. The LiDAR sensor captures high-fidelity 3D structural information, which can be represented by various formats, i.e., points [4], [5], [8], range view [16], [15], [11], [12], [21], voxels [27], [28], [7], bird’s eye view (BEV) [29], hybrid [18], [19] and multi-modal representations [30], [3], [31]. There are also some works [3], [30] that fuse multi-sensor information. The point and voxel methods are prevailing, but their complexity is $\mathcal{O}(N \cdot d)$ where N is in the order of 10^5 [20]. Thus, most approaches are not suitable for robotics or autonomous driving applications. The BEV method [29] offers a more efficient choice with $\mathcal{O}(\frac{H \cdot W}{r^2} \cdot d)$ complexity, but the accuracy is sub par [21]. The multi-modal methods require additional resources to process the additional modalities. Among all representations, the range view reflects the LiDAR sampling process and it is much more efficient than other representations with $\mathcal{O}(\frac{H \cdot W}{r^2} \cdot d)$ complexity. We thus focus on the range-view as representation.

Multi-frame LiDAR data processing. Multi-frame information plays a crucial role in LiDAR data processing. For example, MOS [32] and MotionSeg3D [33] generate residual images from multiple LiDAR frames to explore the sequential information and use it for segmenting moving and static objects. Motivated by these approaches, MetaRangeSeg [34] also uses residual range images for the task of semantic segmentation of LiDAR sequences. It employs a meta-kernel to extract the meta features from the residual images. SeqOT [35] exploits sequential LiDAR frames using yaw-rotation-invariant OverlapNets [36], [37] and transformer networks [23], [38] to generate a global descriptor for fast place recognition in an end-to-end manner. In addition, SCPNet [39] designs a knowledge distillation

strategy between multi-frame LiDAR scans and a single-frame LiDAR scan for semantic scene completion. Recently, Mars3D [40] designed a plug-and-play motion-aware module for multi-scan 3D point clouds to classify semantic categories and motion states. Seal [41] proposes a temporal consistency loss to constraint the semantic prediction of super-points from multiple scans. Although the benefit of using multiple scans has been studied, these works address other tasks.

Post processing. Although range-view-based LiDAR segmentation methods are computationally efficient, they suffer from boundary blurriness or the “many-to-one” issue [16], [15] as discussed in Sec. I. To alleviate this issue, most works use a conditional random field (CRF) [16] or k-NN [15] to smooth the predicted labels. [16] implements the CRF as an end-to-end trainable recurrent neural network to refine the predictions according to the predictions of the neighbors within three iterations. It does not address occluded points explicitly. k-NN [15] infers the semantics of ambiguous points by jointly considering its k closest neighbours in terms of the absolute range distance. However, finding a balance between under and over-smoothing can be challenging, and it may not be able to handle severe occlusions. Recently, NLA [12] assigns the nearest point’s prediction in a local patch to the occluded point. However, it requires to iterate over each point to verify occlusions. In addition, RangeFormer [21] addresses this issue by creating sub-clouds from the entire point cloud and inferring labels for each subset. However, partitioning the cloud into sub-clouds ignores the global information. It can also not easily be applied to existing networks. Some methods [42], [33], [43] propose additional refinement modules for the networks to refine the initial estimate, which increases the runtime. In this work, we propose to tackle this issue by combining past predictions in an efficient max-voting manner. Our method complements existing approaches and can be applied to various networks.

III. PROPOSED METHOD

A. Network Overview

The overview of our proposed network is illustrated in Fig. 2. Our proposed network takes as input a point cloud P comprising N points represented by 3D coordinates x, y, z , and intensity i . The point cloud is projected onto a range image I of size $H \times W \times 5$ using a spherical projection technique employed in previous works [15], [16]. Here, H and W represent the height and width of the image, and the last dimension includes coordinates (x, y, z) , range $r = \sqrt{x^2 + y^2 + z^2}$, and intensity i . Next, we feed the range image into our backbone model to obtain multi-scale features F with resolutions $\{1, 1/2, 1/4, 1/8\}$. We employ a **Temporal Cross-Attention (TCA)** layer to integrate spatial features from history frame. The aggregated features are then fed to the segmentation head, which predicts the range-image-based semantic segmentation logits O . For inference, we re-project the 2D semantic segmentation prediction to a 3D point-wise prediction S . Subsequently, we propose a **Max-Voting-based Post-processing (MVP)** strategy to refine

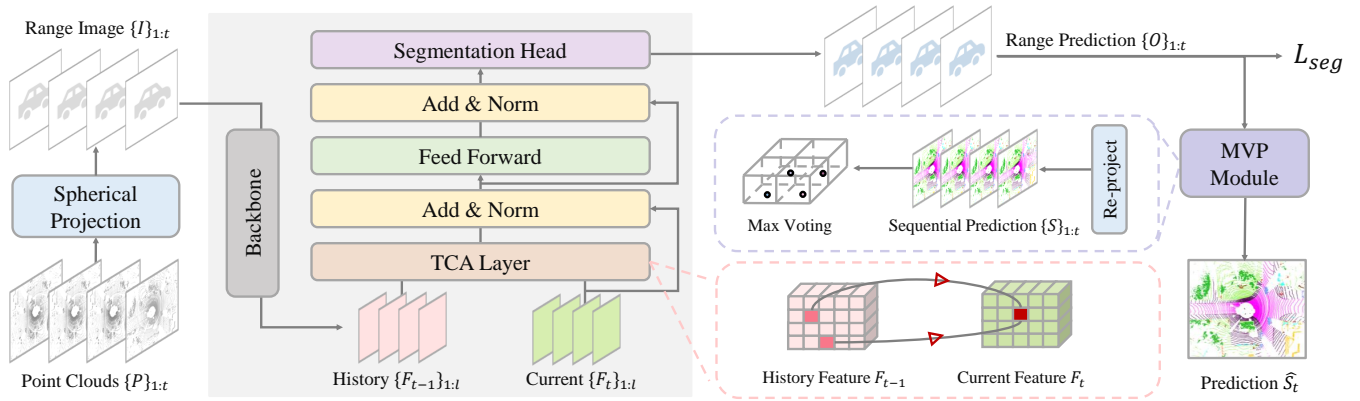


Fig. 2: Architecture of TFNet. For a point cloud P_t , TFNet projects it onto range images I_t . It then uses a segmentation backbone to extract multi-scale features $\{F_t\}_{1:l}$, a **Temporal Cross-Attention (TCA)** layer to integrate past features $\{F_{t-1}\}_{1:l}$, and a segmentation head to predict range-image-based logits O_t . In inference, it refines the re-projected prediction S_t by aggregating the current and past temporal predictions $\{S\}_{1:t}$ by a **Max-Voting-based Post-processing (MVP)** strategy.

the current prediction S_t by aggregating previous predictions. We describe the key components of our network in the following sections.

B. Temporal cross attention

Although the range image suffers from the “many-to-one” issue, the occluded points can be captured from adjacent scans. This observation motivates us to incorporate sequential scans into both the training and inference stages. First, we discuss how sequential data can be exploited during the training stage.

Inspired by the notable information extraction ability of the attention mechanism [23] verified by various works [44], [24], [45], [46], we use the cross-attention mechanism to model the temporal connection between the previous range feature F_{t-1} and the current range feature F_t .

The attended value is computed by:

$$\mathbf{x}_{in} = \text{Attention}(Q, K, V) = \text{Softmax}\left(\frac{Q \cdot K^T}{\sqrt{d_f}}\right) V, \quad (1)$$

where Q, K, V are obtained by $Q = \text{Linear}_q(F_t)$, $K = \text{Linear}_k(F_{t-1})$, $V = \text{Linear}_v(F_{t-1})$, and d_f is the dimension of the range features. We integrate a 3×3 convolution into the feed-forward module to encode positional information as in [44] as well as a residual connection [47]. The **feed-forward module** is defined as follows:

$$\mathbf{x}_{out} = \text{MLP}(\text{GELU}(\text{Conv}_{3 \times 3}(\text{MLP}(\mathbf{x}_{in})))) + \mathbf{x}_{in}. \quad (2)$$

The TCA module effectively exploits temporal dependencies in two ways. First, instead of using multiple stacked range features [32], our method extracts temporal information from the previous range features. This not only reduces computational costs but also minimizes the influence of moving objects, which can introduce noise into the data. Secondly, we only utilize the fusion module on the last feature level, which significantly decreases computation complexity. Previous works [24], [25] have shown that the attention at shallower layers is not effective.

C. Max-voting-based post-processing

While temporal cross attention exploits temporal information at the feature level, it does not resolve the “many-to-one” issue during the re-projection process of a range-image-based method, which causes occluded far points to inherit the predictions of near points. We thus propose a max-voting-based post-processing (MVP) strategy, which is motivated by the observation that occluded points will be visible in the adjacent scans as shown in Fig. 1. As verified in Tab. V, MVP is generic and can be added to various networks.

Temporal scan alignment. To initiate post-processing, it is essential to align a series of past LiDAR scans (P_1, \dots, P_t) to the viewpoint (i.e., coordinate frame) of P_t . The alignment is accomplished by utilizing the estimated relative pose transformations T_{j-1}^j between the scans P_{j-1} and P_j . These transformation matrices can be acquired from an odometry estimation approach such as SuMa++ [50]. The relative transformations between the scans (T_1^2, \dots, T_{t-1}^t) are represented by transformation matrices of $T_{j-1}^j \in \mathbb{R}^{4 \times 4}$. Further, we denote the j^{th} scan transformed to the viewpoint of P_t by

$$P^{j \rightarrow t} = \{T_j^t p_i\}_{p_i \in P_j} \quad \text{with} \quad T_j^t = \prod_{k=j+1}^t T_{k-1}^k. \quad (3)$$

Sparse grid max voting. After applying the transformations, we aggregate the aligned scans. We quantize the aggregated scans into a voxel grid with a fixed resolution δ . In each grid, we use the max-voting strategy to use the most frequently predicted class label to represent the semantics of all points in the grid. We illustrate this process in Fig. 3 and evaluate the impact of the grid size in Fig. 6. To save computation and memory, we store only the non-empty voxels. This sparse representation allows our method to handle large scenes.

Sliding window update. We initialize a sliding window $W_{t-L+1:t}$ with the length of L to store the scans and use a FIFO (First In First Out) strategy to update the points falling in each grid. When the LiDAR sensor obtains a new point cloud scan, we add it to this sliding window and remove the

TABLE I: Performance comparison on SemanticKITTI test set.

	Input	mean-IoU	car	bicycle	motorcycle	truck	other-vehicle	person	bicyclist	motorcyclist	road	parking	sidewalk	other-ground	building	fence	vegetation	trunk	terrain	pole	traffic-sign
PointNet [4]	Point	14.6	46.3	1.3	0.3	0.1	0.8	0.2	0.2	0.0	61.6	15.8	35.7	1.4	41.4	12.9	31.0	4.6	17.6	2.4	3.7
PointNet++ [5]		20.1	53.7	1.9	0.2	0.9	0.2	0.9	1.0	0.0	72.0	18.7	41.8	5.6	62.3	16.9	46.5	13.8	30.0	6.0	8.9
LatticeNet [10]		52.9	92.9	16.6	22.2	26.6	21.4	35.6	43.0	46.0	90.0	59.4	74.1	22.0	88.2	58.8	81.7	63.6	63.1	51.9	48.4
RandLA-Net [9]		53.9	94.2	26.0	25.8	40.1	38.9	49.2	48.2	7.2	90.7	60.3	73.7	20.4	86.9	56.3	81.4	61.3	66.8	49.2	47.7
KPConv [8]		58.8	96.0	30.2	42.5	33.4	44.3	61.5	61.6	11.8	88.8	61.3	72.7	<u>31.6</u>	90.5	64.2	84.8	69.2	69.1	56.4	47.4
BAAF-Net [6]		59.9	95.4	31.8	35.5	48.7	46.7	49.5	55.7	33.0	90.9	62.2	74.4	23.6	89.8	60.8	82.7	63.4	67.9	53.7	52.0
MINet [48]	Range	55.2	90.1	41.8	34.0	29.9	23.6	51.4	52.4	25.0	90.5	59.0	72.6	25.8	85.6	52.3	81.1	58.1	66.1	49.0	59.9
FIDNet [12]		59.5	93.9	54.7	48.9	27.6	23.9	62.3	59.8	23.7	90.6	59.1	75.8	26.7	88.9	60.5	84.5	64.4	69.0	53.3	62.8
Meta-RangeSeg [34]		61.0	93.9	50.1	43.8	43.9	43.2	63.7	53.1	18.7	90.6	64.3	74.6	29.2	91.1	64.7	82.6	65.5	65.5	56.3	64.2
KPRNet [42]		63.1	<u>95.5</u>	54.1	47.9	23.6	42.6	65.9	65.0	16.5	93.2	73.9	80.6	30.2	<u>91.7</u>	<u>68.4</u>	85.7	69.8	71.2	58.7	64.1
Lite-HDseg [49]		63.8	92.3	40.0	55.4	37.7	39.6	59.2	<u>71.6</u>	54.1	93.0	68.2	78.3	29.3	91.5	65.0	78.2	65.8	65.1	59.5	<u>67.7</u>
CENet [11]		<u>64.7</u>	91.9	<u>58.6</u>	50.3	40.6	42.3	<u>68.9</u>	65.9	<u>43.5</u>	90.3	60.9	75.1	31.5	91.0	66.2	84.5	69.7	<u>70.0</u>	61.5	67.6
RangeViT [43]		64.0	95.4	55.8	43.5	29.8	42.1	63.9	58.2	38.1	<u>93.1</u>	<u>70.2</u>	<u>80.0</u>	32.5	92.0	69.0	<u>85.3</u>	<u>70.6</u>	71.2	<u>60.8</u>	64.7
LENet [13]		64.5	93.9	57.0	<u>51.3</u>	<u>44.3</u>	<u>44.4</u>	66.6	64.9	36.0	91.8	68.3	76.9	30.5	91.2	66.0	83.7	68.3	67.8	58.6	63.2
TFNet (Ours)		66.1	94.3	60.7	58.5	38.4	48.4	74.3	72.2	35.5	90.6	68.5	75.3	29.0	91.6	67.3	83.8	71.1	67.0	<u>60.8</u>	68.7

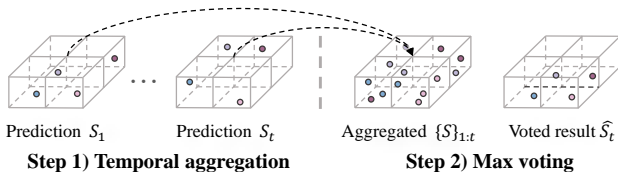


Fig. 3: Illustration of the max voting post-processing strategy. oldest scan. We do not use different weights across frames due to the uncertain occlusion problem.

IV. EXPERIMENTS

Datasets and evaluation metrics. We use two benchmark datasets, SemanticKITTI [1] and SemanticPOSS [26], to evaluate our proposed method. SemanticKITTI [1] is a popular benchmark for LiDAR-based semantic segmentation in driving scenes. It contains 19,130 training frames, 4,071 validation frames, and 20,351 test frames. Each point in the dataset is provided with a semantic label of 19 classes for semantic segmentation. We also evaluate our dataset on the SemanticPOSS [26] dataset, which contains 2988 scenes for training and testing. For evaluation, we follow previous works [11], [21], [12], [16], utilizing the class-wise Intersection over Union (IoU) and mean IoU (mIoU) metrics to evaluate and compare with others.

Implementation details. While we use CENet [11] as the main baseline method, our method demonstrates robust generalization across various backbones as shown in the following experiments. We train the proposed method using the Stochastic Gradient Descent (SGD) optimizer and set the batch size to 8 and 4 for SemanticKITTI and SemanticPOSS, respectively. We follow the baseline method [11] to supervise the training with a weighted combination of cross-entropy, Lovász softmax loss [51], and boundary loss [52]. The weights for the loss terms are set to $\beta_1 = 1.0$, $\beta_2 = 1.5$, $\beta_3 = 1.0$, respectively. All the models are trained on GeForce RTX 3090 GPUs. The inference latency is measured using a single GeForce RTX 3090 GPU. The backbone is trained

TABLE II: Evaluation results on the SemanticPOSS test set.

	Sq.Seg [16]	Sq.SegV2 [53]	RangeNet [15]	MINet [48]	FIDNet [12]	CENet [11]	TFNet (Ours)
person	6.8	43.9	57.3	62.4	72.2	75.5	<u>72.4</u>
rider	0.6	7.1	4.6	12.1	23.1	<u>22.0</u>	20.5
car	6.7	47.9	35.0	63.8	72.7	<u>77.6</u>	77.7
truck	4.0	18.4	14.1	22.3	23.0	25.3	<u>24.8</u>
plants	2.5	40.9	58.3	68.6	68.0	72.2	<u>71.6</u>
traffic-sign	9.1	4.8	3.9	16.7	<u>22.2</u>	18.2	29.1
pole	1.3	2.8	6.9	30.1	28.6	<u>31.5</u>	37.8
trashcan	0.4	7.4	24.1	28.9	16.3	48.1	<u>46.3</u>
building	37.1	57.5	66.1	75.1	73.1	<u>76.3</u>	79.9
cone/stone	0.2	0.6	6.6	58.6	34.0	27.7	<u>34.5</u>
fence	8.4	12.0	23.4	32.2	40.9	47.7	<u>47.3</u>
bike	18.5	35.3	28.6	44.9	50.3	51.4	53.9
ground	72.1	71.3	73.5	76.3	<u>79.1</u>	80.3	78.4
mean-IoU	12.9	26.9	30.9	43.2	46.4	<u>50.3</u>	51.9

from scratch on all the datasets.

A. Comparison with state-of-the-arts

Quantitative results on SemanticKITTI. Tab. I reports comparisons with representative models on the SemanticKITTI test set. Our method outperforms all range-image-based methods, including CNN-based architectures [11], [12], [48] and Transformer-based architectures [43] in terms of mean IoU. CENet [11] uses test time augmentation to improve the performance. For a fair comparison with previous methods [15], [48], we do not use test time augmentation.

Quantitative results on SemanticPOSS. We present our performance on the SemanticPOSS test set [26] in Tab. II. Our approach outperforms all approaches in terms of mean IoU. Compared to CENet, our method shows a significant advantage in predicting small objects such as traffic signs, poles, and cones/stones.

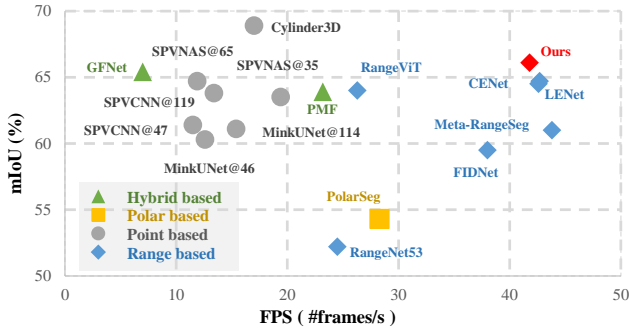


Fig. 4: mIoU vs. runtime on SemanticKITTI. Our method balances mIoU and inference time better than other state-of-the-art methods. Best viewed in color.

Inference time comparison. We visualize the inference time and mIoU of popular methods in Fig. 4. The results show that range-image-based methods are faster than point, polar, or hybrid methods. We measured the inference time of all the methods on the same hardware with a GeForce RTX 3090 GPU for a fair comparison.

B. Ablation Analysis

Effect of the temporal post-processing. Tab. III compares the proposed post-processing method with other post-processing approaches on the SemanticKITTI validation set. Using a CRF for post-processing has been used by SqueezeSegv2 [53]. We train the network with CRF from scratch using the same training pipeline as our method. The k-Nearest Neighbor (k-NN) method [15] is the most popular post-processing method. It is widely used in Lite-HDseg [49], SqueezeSegv3 [54], CENet [11], SalsaNext [14], and MiNet [48]. The Nearest Label Assignment (NLA) post-processing is used by FIDNet [12]. It iterates over each point to check if a point is occluded or not. We use the source code from the corresponding methods. For the Point Refine module proposed in MotionSeg3D [33], we follow its implementation. We use SPVCNN [7] as the Point Refine module and use the features before the classification layer as the input to the Point Refine module. We then fine-tune the network with the Point Refine module in a second stage with a 0.001 learning rate for ten epochs. The results show the “many-to-one” issue harms the performance heavily. Without our proposed post-processing (‘w/o MVP’), mean IoU is by 6.1 lower. That CRF can actually decrease the mean IoU has been also shown in [15]. While NLA and k-NN improve the results, the best mean IoU is achieved by our approach.

Effect of different fusion strategy. In Tab. IV, we replace the proposed temporal fusion layer with other strategies. Mars3D [40] adopts element-wise summation to aggregate temporal multi-scan point cloud embeddings and produce enhanced features. The temporal memory attention (TMA) module [55] validates its effectiveness on the video semantic segmentation task. BEVFormer v2 [56] uses a feature warp and concatenation strategy to incorporate temporal information and shows its effectiveness on the LiDAR detection task. We follow its implementation, which concatenates previous

BEV features with the current BEV feature along the channel dimension and employs residual blocks for dimensionality reduction. We transform the scans to the same ego-car coordinates to implement the accurate alignment between temporal scans. For the LiDAR semantic segmentation task, Meta-RangeSeg [34] proposes to use three previous residual images as input and a meta-kernel module to incorporate temporal information. We follow its implementation and add to the five-channel input (x,y,z,r,i) three channels for the three residual images and a channel for the mask, which indicates whether the pixel is a projected 3D point or not. The residual images are calculated by first transforming the point clouds of previous frames into the coordinates of the current frame and then calculating the absolute differences between the range values of the current scan and the transformed one with normalization. A meta-kernel is followed to capture the spatial and temporal information. For a fair comparison, we keep the encoder and decoder of our architecture. We report the projection-based mIoU here because the loss function is applied directly to the range image. All strategies are trained with the same setting and pipeline. The results in Tab. IV show that our temporal fusion approach performs best.

C. Generalization Ability

In order to demonstrate that the proposed max-voting-based post-processing (MVP) can be applied to other networks, we apply MVP to various networks including point-based methods [27], [7], range-image-based methods [34], [11], [12], and a polar-based method [17]. In contrast to Tab. I, which contains the reported results on the test set, Tab. V reports the results of the public available pre-trained models with and without post-processing on the validation set. The results show that the proposed MVP post-processing improves the results for various approaches.

D. Further Analysis

Effect of frame numbers. In Fig. 6 (a), we analyze the impact of the length L of the sliding window update discussed in Sec. III-C. It shows that $L = 10$ is a reasonable choice.

Effect of grid size resolution. As discussed in Sec. III-C, we quantize the aggregated scans into a voxel grid with a fixed resolution. Note that the resolution needs to be appropriate since the underlying assumption is that all points inside a voxel share the same semantic class. This assumption is violated if the voxel size is too large and the estimates become noisy when it is too small. We evaluate the impact of different resolutions in Fig. 6 (b). The results show that a voxel size of 0.10m works best.

Qualitative evaluation. We provide a visual comparison of two point clouds in Fig. 5. The impact of the “many-to-one” problem is evident when there is no post-processing technique applied, shown in Fig. 5 (a). Specifically, points of the trunk of the tree inherit the predictions from points of the traffic sign and vegetation since they are projected to the same range pixel. In Fig. 5 (b), the widely-used k-NN [15] refines the predictions, but it cannot correct false predictions when larger areas are occluded. In contrast,

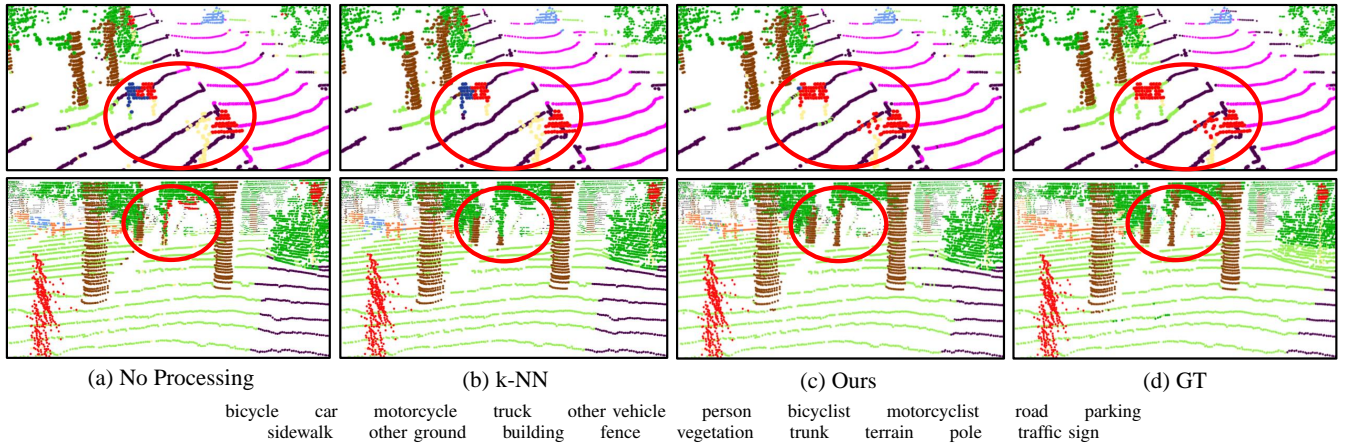


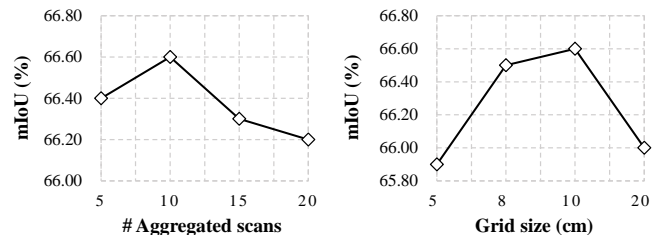
Fig. 5: Qualitative analysis of the post-processing scheme. (a) The “many-to-one” issue is evident without post-processing, e.g., the trunk is partially segmented as traffic sign and vegetation as they project onto the same range pixel (row 2). (b) k-NN [15] smooths the semantic labels locally, but it cannot resolve ambiguities by objects that are close or prediction errors. (c) Our method exploits temporal information to resolve false predictions (row 1) or ambiguities due to occlusions (row 2). Best viewed in color.

TABLE III: Comparison with different post-processing methods. Our MVP method is significantly better.

	mean-IoU	car	bicycle	motorcycle	truck	other-vehicle	person	bicyclist	motorcyclist	road	parking	sidewalk	other-ground	building	fence	vegetation	trunk	terrain	pole	traffic-sign
w/o MVP	60.4	85.8	44.0	61.5	80.3	53.0	68.7	70.2	0.91	94.8	42.1	80.9	0.95	81.8	52.4	83.2	60.3	70.6	51.9	47.9
CRF [16]	58.2 (-2.2)	87.0	40.0	57.3	67.7	52.2	66.1	62.5	0.38	94.5	46.4	81.1	0.66	81.7	53.6	81.4	60.9	66.3	49.0	47.6
PointRefine [33]	59.2 (-1.2)	84.5	43.7	53.7	76.3	48.6	68.3	70.6	<u>7.5</u>	94.6	39.8	80.5	11.8	81.4	50.7	83.8	59.4	<u>72.2</u>	51.1	46.1
NLA [12]	64.4 (+4.0)	92.0	47.5	66.8	79.0	<u>55.9</u>	76.2	<u>85.7</u>	12.4	94.5	42.7	80.8	<u>10.6</u>	87.3	54.6	85.9	66.0	<u>72.2</u>	63.4	49.8
k-NN [15]	64.5 (+4.1)	91.4	<u>50.7</u>	<u>66.9</u>	<u>81.2</u>	54.9	<u>76.8</u>	85.1	0.96	94.5	41.6	80.9	0.95	88.5	<u>55.6</u>	<u>86.2</u>	<u>66.8</u>	71.5	<u>64.5</u>	<u>50.2</u>
MVP (Ours)	66.5 (+6.1)	93.4	54.1	70.2	85.9	59.8	79.8	88.0	0.58	<u>94.7</u>	<u>44.8</u>	81.1	0.46	90.3	66.6	86.8	69.5	72.7	65.1	50.3

TABLE IV: Comparison with other temporal fusion methods.

Fusion Strategies	mIoU
w/o TCA	66.9
TMA module [55]	67.8 (+0.9)
Residual images [34]	61.4 (-5.5)
Element-wise addition [40]	67.6 (+0.7)
Channel concatenation [56]	<u>68.0 (+1.1)</u>
TCA module (ours)	68.1 (+1.2)



(a) Effect of number of scans. (b) Effect of grid size.

Fig. 6: Effect of window size and grid size resolution.

TABLE V: Generalization to other networks.

Backbone	Input	Post-processing	
		-	MVP (Ours)
MinkUNet [27]	Point	58.9	/
SPVNAS [7]		64.7	/
FIDNet [12]	Range	55.4	<u>58.6 (+3.2)</u>
Meta-RangeSeg [34]		56.6	<u>60.3 (+3.7)</u>
CENet [11]	Polar	58.8	<u>62.6 (+3.8)</u>
PolarSeg [17]		57.2	/
			61.5 (+6.1)
			63.1 (+6.5)
			64.7 (+5.9)
			58.0 (+0.8)

our method corrects false predictions in the single scan by keeping a consistent prediction across previous scans, as shown in Fig. 5 (c). This demonstrates the benefit of introducing temporal information in the post-processing step to resolve the “many-to-one” problem.

V. CONCLUSION

In this paper, we introduced a novel solution named TFNet to tackle the issue of boundary blurriness, also called “many-to-one”, in range-image-based LiDAR semantic segmentation tasks. Our approach leverages temporal information by proposing temporal fusion layers during the training process and a sequential max voting strategy during inference. The experiments on two benchmarks demonstrate the advantages of TFNet. In particular, integrating temporal information enables TFNet to exhibit robustness in scenarios with significant occlusion while maintaining real-time performance. Furthermore, we conducted comprehensive ablation studies to validate the design, as well as the generalization of the proposed post-processing to other networks.

REFERENCES

- [1] J. Behley, M. Garbade, A. Milioto, J. Quenzel, S. Behnke, C. Stachniss, and J. Gall, "Semantickitti: A dataset for semantic scene understanding of lidar sequences," in *ICCV*, 2019.
- [2] H. Caesar, V. Bankiti, A. H. Lang, S. Vora, V. E. Liong, Q. Xu, A. Krishnan, Y. Pan, G. Baldan, and O. Beijbom, "nusenes: A multimodal dataset for autonomous driving," in *CVPR*, 2020.
- [3] Z. Zhuang, R. Li, K. Jia, Q. Wang, Y. Li, and M. Tan, "Perception-aware multi-sensor fusion for 3d lidar semantic segmentation," in *ICCV*, 2021.
- [4] C. R. Qi, H. Su, K. Mo, and L. J. Guibas, "Pointnet: Deep learning on point sets for 3d classification and segmentation," in *CVPR*, 2017.
- [5] C. R. Qi, L. Yi, H. Su, and L. J. Guibas, "Pointnet++: Deep hierarchical feature learning on point sets in a metric space," in *NeurIPS*, 2017.
- [6] S. Qiu, S. Anwar, and N. Barnes, "Semantic segmentation for real point cloud scenes via bilateral augmentation and adaptive fusion," in *CVPR*, 2021.
- [7] Z. Liu, H. Tang, Y. Lin, and S. Han, "Point-voxel cnn for efficient 3d deep learning," in *NeurIPS*, 2019.
- [8] H. Thomas, C. R. Qi, J.-E. Deschuid, B. Marcotegui, F. Goulette, and L. J. Guibas, "Kpconv: Flexible and deformable convolution for point clouds," in *ICCV*, 2019.
- [9] Q. Hu, B. Yang, L. Xie, S. Rosa, Y. Guo, Z. Wang, N. Trigoni, and A. Markham, "Randla-net: Efficient semantic segmentation of large-scale point clouds," in *CVPR*, 2020.
- [10] X. Luo, Y. Xie, Y. Zhang, Y. Qu, C. Li, and Y. Fu, "Latticenet: Towards lightweight image super-resolution with lattice block," in *ECCV*, 2020.
- [11] H.-X. Cheng, X.-F. Han, and G.-Q. Xiao, "Cenet: Toward concise and efficient lidar semantic segmentation for autonomous driving," in *ICME*, 2022.
- [12] Y. Zhao, L. Bai, and X. Huang, "Fidnet: Lidar point cloud semantic segmentation with fully interpolation decoding," in *IROS*, 2021.
- [13] B. Ding, "Lenet: Lightweight and efficient lidar semantic segmentation using multi-scale convolution attention," in *arXiv*, 2023.
- [14] T. Cortinhal, G. Tzelepis, and E. E. Aksoy, "Salsanext: Fast, uncertainty-aware semantic segmentation of lidar point clouds," in *ISVC*, 2020.
- [15] A. Milioto, I. Vizzo, J. Behley, and C. Stachniss, "Rangenet++: Fast and accurate lidar semantic segmentation," in *IROS*, 2019.
- [16] B. Wu, A. Wan, X. Yue, and K. Keutzer, "Squeezeseg: Convolutional neural nets with recurrent crf for real-time road-object segmentation from 3d lidar point cloud," in *ICRA*, 2018.
- [17] Y. Zhang, Z. Zhou, P. David, X. Yue, Z. Xi, and H. Foroosh, "Polarnet: An improved grid representation for online lidar point clouds semantic segmentation," in *arXiv*, 2020.
- [18] H. Qiu, B. Yu, and D. Tao, "GFNet: Geometric flow network for 3d point cloud semantic segmentation," in *Transactions on Machine Learning Research*, 2022.
- [19] X. Li, G. Zhang, H. Pan, and Z. Wang, "Cpynet: Cascade point-grid fusion network for real-time lidar semantic segmentation," in *ICRA*, 2022.
- [20] M. Uecker, T. Fleck, M. Pflugfelder, and J. M. Zöllner, "Analyzing deep learning representations of point clouds for real-time in-vehicle lidar perception," in *arXiv*, 2022.
- [21] L. Kong, Y. Liu, R. Chen, Y. Ma, X. Zhu, Y. Li, Y. Hou, Y. Qiao, and Z. Liu, "Rethinking range view representation for lidar segmentation," in *ICCV*, 2023.
- [22] J. Behley, M. Garbade, A. Milioto, J. Quenzel, S. Behnke, J. Gall, and C. Stachniss, "Towards 3D LiDAR-based semantic scene understanding of 3D point cloud sequences: The SemanticKITTI Dataset," *The International Journal on Robotics Research*, vol. 40, no. 8-9, pp. 959-967, 2021.
- [23] A. Vaswani, N. Shazeer, N. Parmar, J. Uszkoreit, L. Jones, A. N. Gomez, Ł. Kaiser, and I. Polosukhin, "Attention is all you need," in *NeurIPS*, 2017.
- [24] K. Li, Y. Wang, P. Gao, G. Song, Y. Liu, H. Li, and Y. Qiao, "Uni-former: Unified transformer for efficient spatiotemporal representation learning," in *arXiv*, 2022.
- [25] P. Gao, T. Ma, H. Li, Z. Lin, J. Dai, and Y. Qiao, "Mcmae: Masked convolution meets masked autoencoders," in *NeurIPS*, 2022.
- [26] Y. Pan, B. Gao, J. Mei, S. Geng, C. Li, and H. Zhao, "Semanticcpos: A point cloud dataset with large quantity of dynamic instances," in *IV*, 2020.
- [27] C. Choy, J. Gwak, and S. Savarese, "4d spatio-temporal convnets: Minkowski convolutional neural networks," in *CVPR*, 2019.
- [28] X. Zhu, H. Zhou, T. Wang, F. Hong, Y. Ma, W. Li, H. Li, and D. Lin, "Cylindrical and asymmetrical 3d convolution networks for lidar segmentation," in *CVPR*, 2021.
- [29] Q. Chen, S. Vora, and O. Beijbom, "Polarstream: Streaming lidar object detection and segmentation with polar pillars," in *NeurIPS*, 2021.
- [30] X. Yan, J. Gao, C. Zheng, C. Zheng, R. Zhang, S. Cui, and Z. Li, "2dpass: 2d priors assisted semantic segmentation on lidar point clouds," in *ECCV*, 2022.
- [31] J. Cen, S. Zhang, Y. Pei, K. Li, H. Zheng, M. Luo, Y. Zhang, and Q. Chen, "Cmdfusion: Bidirectional fusion network with cross-modality knowledge distillation for lidar semantic segmentation," in *arXiv*, 2023.
- [32] X. Chen, S. Li, B. Mersch, L. Wiesmann, J. Gall, J. Behley, and C. Stachniss, "Moving object segmentation in 3d lidar data: A learning-based approach exploiting sequential data," in *R-AL*, 2021.
- [33] J. Sun, Y. Dai, X. Zhang, J. Xu, R. Ai, W. Gu, and X. Chen, "Efficient spatial-temporal information fusion for lidar-based 3d moving object segmentation," in *IROS*, 2022.
- [34] S. Wang, J. Zhu, and R. Zhang, "Meta-rangeseg: Lidar sequence semantic segmentation using multiple feature aggregation," in *R-AL*, 2022.
- [35] J. Ma, X. Chen, J. Xu, and G. Xiong, "Seqot: A spatial-temporal transformer network for place recognition using sequential lidar data," in *IEEE Transactions on Industrial Electronics*, 2022.
- [36] X. Chen, T. Labe, A. Milioto, T. Röhling, O. Vysotska, A. Haag, J. Behley, and C. Stachniss, "OverlapNet: Loop Closing for LiDAR-based SLAM," in *RSS*, 2020.
- [37] X. Chen, T. Labe, A. Milioto, T. Röhling, J. Behley, and C. Stachniss, "OverlapNet: A Siamese Network for Computing LiDAR Scan Similarity with Applications to Loop Closing and Localization," in *Autonomous Robots*, 2021.
- [38] J. Ma, J. Zhang, J. Xu, R. Ai, W. Gu, and X. Chen, "Overlaptransformer: An efficient and yaw-angle-invariant transformer network for lidar-based place recognition," in *R-AL*, 2022.
- [39] Z. Xia, Y. Liu, X. Li, X. Zhu, Y. Ma, Y. Li, Y. Hou, and Y. Qiao, "Sepnet: Semantic scene completion on point cloud," in *CVPR*, 2023.
- [40] J. Liu, C. Chang, J. Liu, X. Wu, L. Ma, and X. Qi, "Mars3d: A plug-and-play motion-aware model for semantic segmentation on multi-scan 3d point clouds," in *CVPR*, 2023.
- [41] Y. Liu, L. Kong, J. Cen, R. Chen, W. Zhang, L. Pan, K. Chen, and Z. Liu, "Segment any point cloud sequences by distilling vision foundation models," in *arXiv*, 2023.
- [42] D. Kochanov, F. K. Nejadasl, and O. Booij, "Kprnet: Improving projection-based lidar semantic segmentation," in *arXiv*, 2020.
- [43] A. Ando, S. Gidaris, A. Bursuc, G. Puy, A. Boulch, and R. Marlet, "Rangevit: Towards vision transformers for 3d semantic segmentation in autonomous driving," in *CVPR*, 2023.
- [44] E. Xie, W. Wang, Z. Yu, A. Anandkumar, J. M. Alvarez, and P. Luo, "Segformer: Simple and efficient design for semantic segmentation with transformers," in *NeurIPS*, 2021.
- [45] M. Wang, T. Ma, X. Zuo, J. Lv, and Y. Liu, "Correlation pyramid network for 3d single object tracking," in *CVPR*, 2023.
- [46] T. Ma, M. Wang, J. Xiao, H. Wu, and Y. Liu, "Synchronize feature extracting and matching: A single branch framework for 3d object tracking," *arXiv*, ICCV.
- [47] K. He, X. Zhang, S. Ren, and J. Sun, "Deep residual learning for image recognition," in *CVPR*, 2016.
- [48] S. Li, X. Chen, Y. Liu, D. Dai, C. Stachniss, and J. Gall, "Multi-scale interaction for real-time lidar data segmentation on an embedded platform," in *R-AL*. IEEE, 2021.
- [49] R. Razani, R. Cheng, E. Taghavi, and L. Bingbing, "Lite-hdseg: Lidar semantic segmentation using lite harmonic dense convolutions," in *ICRA*, 2021.
- [50] X. Chen, A. M. E. Palazzolo, P. Giguère, J. Behley, and C. Stachniss, "Suma++: Efficient lidar-based semantic slam," in *IROS*, 2019.
- [51] M. Berman, A. R. Triki, and M. B. Blaschko, "The lovasz-softmax loss: a tractable surrogate for the optimization of the intersection-over-union measure in neural networks," in *CVPR*, 2018.
- [52] A. Bokhovkin and E. Burnaev, "Boundary loss for remote sensing imagery semantic segmentation," in *ISNN*, 2019.

- [53] B. Wu, X. Zhou, S. Zhao, X. Yue, and K. Keutzer, "Squeezesegv2: Improved model structure and unsupervised domain adaptation for road-object segmentation from a lidar point cloud," in *ICRA*, 2019.
- [54] C. Xu, B. Wu, Z. Wang, W. Zhan, P. Vajda, K. Keutzer, and M. Tomizuka, "Squeezesegv3: Spatially-adaptive convolution for efficient point-cloud segmentation," in *ECCV*, 2020.
- [55] H. Wang, W. Wang, and J. Liu, "Temporal memory attention for video semantic segmentation," in *ICIP*, 2021.
- [56] C. Yang, Y. Chen, H. Tian, C. Tao, X. Zhu, Z. Zhang, G. Huang, H. Li, Y. Qiao, L. Lu, *et al.*, "Bevformer v2: Adapting modern image backbones to bird's-eye-view recognition via perspective supervision," in *CVPR*, 2023.